ASC Report No. 32/2017

Post-Newtonian equations of motion for LEO debris objects and space-based Acquisition, Pointing and Tracking laser systems

J.M. Gambi, M.L. Garcia del Pinto, J. Schwindl, E.B. Weinmüller

Institute for Analysis and Scientific Computing
Vienna University of Technology — TU Wien
www.asc.tuwien.ac.at ISBN 978-3-902627-00-1

Most recent ASC Reports

31/2017 *J. Burkotova. I. Rachunkova, E.B. Weinmüller*
On singular BVPs with unsmooth data: Analysis of the linear case with variable coefficient matrix

30/2017 *J. Burkotova. I. Rachunkova, E.B. Weinmüller*
On singular BVPs with unsmooth data. Part 2: Convergence of the collocation schemes

29/2017 *G. Hrkac, C.-M. Pfeiler, D. Praetorius, M. Ruggeri, A. Segatti, and B. Stiftner*
Convergent tangent plane integrators for the simulation of chiral magnetic skyrmion dynamics

28/2017 *G. Kitzler and J. Schöberl*
A polynomial spectral method for the spatially homogeneous Boltzmann equation in 3 dimensions

27/2017 *G. Di Fratta, C.-M. Pfeiler, D. Praetorius, M. Ruggeri, B. Stiftner*
Linear second-order IMEX-type integrator for the (eddy current) Landau-Lifshitz-Gilbert equation

26/2017 *F. Achleitner, A. Arnold, and E.A. Carlen*
On multi-dimensional hypocoercive BGK models

25/2017 *M. Braukhoff*
Semiconductor Boltzmann-Dirac-Benny equation with BGK-type collision operator: Existence of solutions vs. ill-posedness

24/2017 *E. Weinmüller*
Numerical simulation of flow in liquid crystals using MATLAB software

23/2017 *X. Chen and A. Jüngel*
Global renormalized solutions to reaction-cross-diffusion systems

22/2017 *A. Sokolova and H. Woracek*
Proper semirings and proper convex functors

Institute for Analysis and Scientific Computing
Vienna University of Technology
Wiedner Hauptstraße 8–10
1040 Wien, Austria

E-Mail: admin@asc.tuwien.ac.at
WWW: http://www.asc.tuwien.ac.at
FAX: +43-1-58801-10196

ISBN 978-3-902627-00-1

Post-Newtonian equations of motion for LEO debris objects and space-based Acquisition, Pointing and Tracking laser systems

J.M. Gambi[a,*], M.L. García del Pino[a], J. Gschwindl[b], E. B. Weinmüller[b]

[a] *Gregorio Millán Institute, Universidad Carlos III de Madrid, 28911 Leganés, Madrid, Spain*
[b] *Institute for Analysis and Scientific Computing, Vienna University of Technology, A-1040 Wien, Austria*

Abstract

This paper deals with the problem of throwing middle-sized low Earth orbit debris objects into the atmosphere via laser ablation. The post-Newtonian equations here provided allow (hypothetical) space-based acquisition, pointing and tracking systems endowed with very narrow laser beams to reach the pointing accuracy presently prescribed. In fact, whatever the orbital elements of these objects may be, these equations will allow the operators to account for the corrections needed to balance the deviations of the line of sight directions due to the curvature of the paths the laser beams are to travel along. To minimize the respective corrections, the systems will have to perform initial positioning manoeuvres, and the shooting point-ahead angles will have to be adapted in real time. The enclosed numerical experiments suggest that neglecting these measures will cause fatal errors, due to differences in the actual locations of the objects comparable to their size.

Keywords: Space-based APT laser systems, LEO space debris, relative motions, Earth post-Newtonian framework.

1. Introduction

It is well known that shielding and avoidance manoeuvres prevent Earth satellites from potential damage produced by small and large debris objects respectively. It is in fact the collisions with middle-sized objects, whose size ranges between 1 cm and 10 cm, the main concern at present, as causing the most serious damage to the satellites. The post-Newtonian (p-N) equations provided in this paper will allow the operators to reach the prescribed pointing accuracy for future acquisition, pointing and tracking (APT) systems endowed with very narrow laser beams to throw into the atmosphere object of this size in low Earth orbit (LEO) by means of laser ablation.

The paper is motivated by recent research activities in solving this problem, in particular, [1, 2, 3, 4]. Detailed descriptions of the problem can be found in [1, 5, 6, 7, 8, 9, 10], see also [11, 12, 13], and a benchmark for our discussion is [14].

According to those authors, removing space debris is a significant highly actual problem, which in future will steadily gain in relevance.

In fact, there are hundreds of thousand of middle-sized pieces of debris in LEO orbits that cannot be tracked by the current sensor networks. This represents a serious invisible threat that may involve nearly a million potential impacts, capable of damaging active satellites, or leading to loss of function after collisions.

Hence, there is a growing consensus to develop space-based APT laser systems aiming at removing these objects in order to ensure a safe future for space activities [1, 6, 12]. [1]

However, the state of constructive measures to carry on with this program is not satisfactory. At present, neither such systems, nor practical activities leading to establishing them in space, are available.

On the other hand, removal of debris per laser ablation can be considered as the best method to solve the problem [1, 4, 8, 9, 13]; see also [10] and [11], as a motivation of the autonomous shooting proposed in [15].

*Corresponding author
Email address: gambi@math.uc3m.es (J.M. Gambi)

[1] Ground-based systems seem not to be suitable to acquire and track middle-sized objects. This is due to the poor initial estimation of their orbital elements. Other restriction is related to passing high power radiation through the atmosphere which may result in loss of the optical quality of the laser beams. Moreover, these systems cannot be used in cloudy conditions and the power of the laser beams required to reach the objects from the Earth surface is too large due to the long distances, [1, 7].

In fact, from the performance models discussed in [1, 2, 3, 4], which are very promising, and from other related publications, such as [12], we can conclude that laser technology for use by future space-based systems has substantially matured during the recent years.

Moreover, pointing technology must have matured even more; for, while there are detailed descriptions of lasers potentially suitable for decaying of such objects into the atmosphere via laser ablation, see [2, 3, 4], data related to pointing accuracy are hardly available.

Looking at available material, two conclusions can be drawn: from [3], that with one laser and one 2.44 m diameter mirror, the diameter of the beam spot at focusing distances below 100 km is smaller than 15 cm; and from [12], that with one laser and one 3 m diameter mirror, the diameter of the beam spot at focusing distances below 250 km is smaller than 11 cm.

Consequently, if the objects of interest are to be removed by focussing on them laser beams with spot sizes at the centimeter level, suitable pointing procedures that include corrections at this level of accuracy are necessary.

Hence, the aim of the present work is to show that the p-N *non-linear equations* for the relative motions introduced in [16] are essential to guarantee the required accuracy.

Here, some remarks are in place to put this paper in a global perspective.

First of all, we show that these equations provide corrections to the Newtonian locations that cannot be derived by using Newtonian methods, or by simple p-N *linear equations*, see [17, 18, 19]. Moreover, we show that under any circumstance of interest, the size of the p-N corrections is similar to the size of the objects involved. And finally, we demonstrate that using the autonomous shooting procedure proposed in [15] minimizes the pointing corrections in real time. In summary, this paper is the last step in a development initiated with [19].

The possible success in applying the derived corrections can be supported by the following facts: (i) the p-N equations suit the recommendation made in [14]; (ii) the results fit perfectly well with those of related research e.g in Space Geodesy [20], Positioning [21], Navigation [22, 23, 24], and Geolocation [25, 26, 27, 28], and (iii) the equations account for the deviations of the line of sight (LOS) directions, derived by Synge, due to the curvature of space along the paths that the narrow laser beams travel along, see [29] and Section 3.

The recommendation by Montenbruck and Gill could already be found in the popular book *Satellite Orbits*, 1st. Edition (2000), and refers to Space Geodesy, but it can obviously be extended to the problem at hand. It says: 'As a rough rule, the size of general relativistic effect is given by the Schwarzschild radius of the Earth $(2GM_{\oplus})/c^2 \approx 1$ cm. Any application in satellite geodesy that approaches this level of accuracy must carefully consider the effects of general relativity.'

The paper is organized as follows. The global space-time metric and the orbital equation based on the geodesic principle used to analyze time-delays and perigee advances, [20, 22, 25, 28], are introduced in Section 2. A detailed description of the structure of the metric about the APT systems and the characteristics of the p-N equations for the relative motions can be found in Section 3. We refer the reader to the complete derivation of these equations to Appendix A. The report on the numerical simulations showing the size of the p-N corrections, as well as the procedure that allows to minimize these corrections, are in Section 4. We complete the paper by conclusions and recommendation on how to increase the pointing accuracy, see Section 5.

2. Initial Observations

An important observation made in many papers cited above, is that to achieve accuracy at the centimeter level while determining positions of middle-sized LEO debris objects, it is necessary to assume that the structure of the space-time about the Earth is described by the second order p-N approximation to the Earth Schwarzschild field, cf. e.g. [14].

According to Synge [29], this structure in Earth Centered Inertial (ECI) coordinates (x_α, x_4), α=1, 2, 3; $G = c = 1$, is given by

$$\begin{aligned} g_{\alpha\beta} &= \delta_{\alpha\beta} + \gamma_{\alpha\beta} + O(\varepsilon^2), \\ g_{\alpha 4} &= O(\varepsilon^{3/2}), \\ g_{44} &= -1 + \gamma_{44} + O(\varepsilon^2), \end{aligned} \tag{1}$$

where

$$\gamma_{\alpha\beta} = \frac{2m}{r}\frac{x_\alpha x_\beta}{r^2}, \quad \gamma_{44} = \frac{2m}{r}. \tag{2}$$

Here, m is the mass of the Earth and $r^2 = x_\alpha x^\alpha$; m and r are measured in seconds, and $\varepsilon \sim O(m/r) \sim O(v^2)$, where v is the characteristic speed of the objects involved; therefore, v is dimensionless.[2]

This assumption implies that the ECI equations of motion for small objects can be derived from the well-known geodesic equations, in which the gravitational

[2]Note that, because (x_α, x_4) are ECI coordinates, $x^\alpha = x_\alpha$, $x^4 = -x_4$, $\gamma^{ij} = \gamma_{ij} + O(\varepsilon^2)$ and $g^{ij} = \eta^{ij} - \gamma^{ij}$ up to $O(\varepsilon^2)$.

force is given by the Christoffel symbols corresponding to this approximation, Eq. (A.4).

Hence, from (1), (2), and (A.1), (A.4), with (A.5) relaxed to $O(\varepsilon)$, see (A.16), (A.17), it follows that the p-N orbital equations in (x^α, x^4), $\alpha = 1, 2, 3$, or (x, y, z, t) are, up to $O(\varepsilon^3)$, [3]

$$\frac{d^2x}{dt^2} = \frac{-m}{r^3}\left[1 + \left(2 - \frac{3x^2}{r^2}\right)\left(\frac{dx}{dt}\right)^2 + \left(2 - \frac{3y^2}{r^2}\right)\left(\frac{dy}{dt}\right)^2 + \left(2 - \frac{3z^2}{r^2}\right)\left(\frac{dz}{dt}\right)^2 - \frac{6xy}{r^2}\frac{dx}{dt}\frac{dy}{dt} - \frac{6xz}{r^2}\frac{dx}{dt}\frac{dz}{dt} - \frac{6yz}{r^2}\frac{dy}{dt}\frac{dz}{dt}\right]x,$$

$$\frac{d^2y}{dt^2} = \frac{-m}{r^3}\left[1 + \left(2 - \frac{3x^2}{r^2}\right)\left(\frac{dx}{dt}\right)^2 + \left(2 - \frac{3y^2}{r^2}\right)\left(\frac{dy}{dt}\right)^2 + \left(2 - \frac{3z^2}{r^2}\right)\left(\frac{dz}{dt}\right)^2 - \frac{6xy}{r^2}\frac{dx}{dt}\frac{dy}{dt} - \frac{6xz}{r^2}\frac{dx}{dt}\frac{dz}{dt} - \frac{6yz}{r^2}\frac{dy}{dt}\frac{dz}{dt}\right]y,$$

$$\frac{d^2z}{dt^2} = \frac{-m}{r^3}\left[1 + \left(2 - \frac{3x^2}{r^2}\right)\left(\frac{dx}{dt}\right)^2 + \left(2 - \frac{3y^2}{r^2}\right)\left(\frac{dy}{dt}\right)^2 + \left(2 - \frac{3z^2}{r^2}\right)\left(\frac{dz}{dt}\right)^2 - \frac{6xy}{r^2}\frac{dx}{dt}\frac{dy}{dt} - \frac{6xz}{r^2}\frac{dx}{dt}\frac{dz}{dt} - \frac{6yz}{r^2}\frac{dy}{dt}\frac{dz}{dt}\right]z. \tag{3}$$

3. Equations of Motion

The p-N equations for the relative motion of any debris object, D, with respect to any space-based APT system, S, cannot be correctly derived by following the classical approach. That is to say, from the assumption that the relative position of D with respect to S is the difference of the ECI p-N positions of D and S. The positions so derived are not reliable [17].

The reason is that, according to General Relativity, the space surrounding the Earth is curved and not flat. Moreover, according to this paradigm, the curvature of space about the Earth is different at different locations.

Hence, the ranging and angle measurements to be made by S will depend not only on the predicted p-N orbital position of S, but also (and at least) on the curvature of space at the spots occupied by S, as well as on the velocity of S.

This conclusion is primarily taken into account by the metric in (A.7), which is the most simple metric that describes the geometry of the neighboring space of S, as seen from S [18, 30].

Now, it follows that only close to S – too close in terms of accuracy and security – the geometry surrounding S is suitably described by this metric.

In fact, the associated geometry is not sufficiently precise for our purpose, since, according to [3, 12], S has to reach D at a long distance by means of a very narrow laser beam. Furthermore, reaching D close to the atmosphere will become rather cumbersome, since the closer D is to the atmosphere, the larger the speed of D and the curvature of space will be.

This means that for any narrow laser beam to reach objects within operative distances, like those mentioned in the Introduction, see [3, 12], the pointing accuracy provided by (A.8) has to be increased by assuming that both the ranging and angle measurements made by S will depend on more variables than those considered in deriving (A.7).

More precisely, we must assume that these measurements will depend not only on the curvature of space at the spots occupied by S, and on the velocity of S in those spots, but also on the curvature at all spots of the virtual segments that will join, while orbiting, the positions of S and D, as well as on the velocity of D.

This is the essential and subtle conclusion that was derived by Synge already in 1960 (!) [29], and it is also the most fruitful assumption in the present paper, since those segments are the LOS's up to $O(\varepsilon)$.

We conclude then that in order to any pointing procedure can account for the p-N corrections to the Newtonian predictions for LEO debris object at realistic and safe distances, the geometry about S must be the one in (A.9). In fact, this is the only structure that allows to satisfy this requirement, by means of the integrals in (A.10), which are to be taken along the segments joining the successive spots occupied by S and D, say $[S, D]$.

Thus, we finally arrive at the p-N structure within the Schwarzschild field up to $O(\varepsilon^2)$, suggested by Montenbruck and Gill, and obtain the following p-N equations of motion of D's with respect to S's. They are now to be used to derive the corrections in local Fermi quasi-Cartesian coordinates, $X^{(\alpha)} = X_{(\alpha)} = (x^\alpha_D - x^\alpha_S) + O(\varepsilon) = ((x_\alpha)_D - (x_\alpha)_S) + O(\varepsilon)$, where $x^\alpha_D = (x_\alpha)_D$ and $x^\alpha_S = (x_\alpha)_S$ are the ECI space coordinates of D and S, respectively

[3] Eq. (3) are scaled such that the ECI coordinates of the debris objects and APT systems are measured in seconds ($c = G = 1$). This simplifies the derivation of the mathematical model and the numerical testing. Thus, we have $m = 1.479 \times 10^{-11}$ s, as in [29], and semi-major axes between 2.192×10^{-2} s and 2.792×10^{-2} s for altitudes from 200 to 2000 km. Finally, the orbital speeds are around 2.629×10^{-5}, so that ε is 10^{-10}.
For completeness and for reader convenience, input data and results are recalculated to standard SI units in Section 4.

(see [16, 29], (A.20), and footnote 2). The equations are

$$\begin{aligned}
\frac{d^2X_{(1)}}{ds^2} &= A_{11}X^{(1)} + A_{12}X^{(2)} + A_{13}X^{(3)} \\
&+ \bar{A}_{11}(X^{(1)})^2 + \bar{A}_{12}X^{(1)}X^{(2)} + \bar{A}_{13}X^{(1)}X^{(3)} \\
&+ \bar{A}_{21}X^{(2)}X^{(1)} + \bar{A}_{22}(X^{(2)})^2 + \bar{A}_{23}X^{(2)}X^{(3)} \\
&+ \bar{A}_{31}X^{(3)}X^{(1)} + \bar{A}_{32}X^{(3)}X^{(2)} + \bar{A}_{33}(X^{(3)})^2, \\
\frac{d^2X_{(2)}}{ds^2} &= A_{21}X^{(1)} + A_{22}X^{(2)} + A_{23}X^{(3)} \\
&+ \bar{B}_{11}(X^{(1)})^2 + \bar{B}_{12}X^{(1)}X^{(2)} + \bar{B}_{13}X^{(1)}X^{(3)} \\
&+ \bar{B}_{21}X^{(2)}X^{(1)} + \bar{B}_{22}(X^{(2)})^2 + \bar{B}_{23}X^{(2)}X^{(3)} \\
&+ \bar{B}_{31}X^{(3)}X^{(1)} + \bar{B}_{32}X^{(3)}X^{(2)} + \bar{B}_{33}(X^{(3)})^2, \\
\frac{d^2X_{(3)}}{ds^2} &= A_{31}X^{(1)} + A_{32}X^{(2)} + A_{33}X^{(3)} \\
&+ \bar{C}_{11}(X^{(1)})^2 + \bar{C}_{12}X^{(1)}X^{(2)} + \bar{C}_{13}X^{(1)}X^{(3)} \\
&+ \bar{C}_{21}X^{(2)}X^{(1)} + \bar{C}_{22}(X^{(2)})^2 + \bar{C}_{23}X^{(2)}X^{(3)} \\
&+ \bar{C}_{31}X^{(3)}X^{(1)} + \bar{C}_{32}X^{(3)}X^{(2)} + \bar{C}_{33}(X^{(3)})^2,
\end{aligned} \tag{4}$$

where s is the proper time of S, i.e., the time recorded by an atomic clock supposedly co-moving with S, and the coefficients $A_{\alpha\gamma}$, $\bar{A}_{\mu\nu}$, $\bar{B}_{\mu\nu}$, and $\bar{C}_{\mu\nu}$ are the integrals in (A.21).

We stress that these integrals have to be computed following the specifications given in (A.12), (A.21). Consequently, the coefficients $A_{\alpha\gamma}$, $\bar{A}_{\mu\nu}$, $\bar{B}_{\mu\nu}$, and $\bar{C}_{\mu\nu}$ in (4), which depend on s, will only be determined after the solutions of (3) for the ECI p-N positions of S and D are available.

Now, to include considering conventional clocks on board S, Eq. (3) have been derived, as indicated in Section 2, by assuming that the relationship between s and t is given by (A.5) up to $O(\varepsilon)$ (see (A.16), (A.17)).

This relationship, together with the structure of space-time shown in (A.9), and the fact that S is assumed to be inertial guided (Eq. (A.6)), are what makes it easy to install Eqs. (3) and (4) into the procedures in [1, 2, 3, 4].

Let us summarize. We can see that Eq. (4) are the basis for a properly working pointing procedure. In fact, the numerical experiments shown below indicate that omitting any of the coefficients in these equations results in fatal errors and the failure of the method. This is due to the fact that the size of the corrections is approximately the size of the objects involved (ranging between 1 cm and 10 cm). In the next section, we shall illustrated that [15] is particularly useful, as long as *none of the coefficients is neglected*.

4. Numerical Experiments

The orbital data considered in the experiments were chosen to be similar to the data found in [1, 2, 3, 4]. Therefore, the p-N corrections computed here can be used to update these procedures.

Hence, all the objects were assumed to be on close circular orbits with altitudes 200 km, 400 km, and 800 km at perigee. This means that we paid particular attention to how the p-N corrections can be used to remove object within the LEO zones of 200 km, 400 km, and 800 km. These zones are relevant, since they are usually dedicated to research satellites, satellites of meteorological monitoring, and distant probing, respectively.[4]

In order to resemble as many potential $S-D$ configurations as possible, the objects were classified into three groups, the *'200 km'*, *'400 km'*, and *'800 km'* group. Each object was identified within one group.

Once classified, we first considered those objects orbiting with relatively large eccentricities, from 0.05 to 0.02. Next, to closely recover more frequent orbits, we considered objects with orbital eccentricities smaller than 0.02, up to finish with the circular limit cases, dealt with in [1, 2, 3, 4], cf. footnote 4.

Otherwise, since there was no loss of generality in choosing particular orbital inclinations (the experiments were carried out in a Schwarzschild field), the orbits were assumed to be equatorial.

To show to which extent corrections derived from the standard initial *S–D* configurations, cf. [1, 2, 3, 4], could be decreased, a set of smaller corrections were derived in parallel, starting from the initial $S-D$ configurations for which a sequence of autonomous shooting could be implemented according to the procedure in [15].

To finally analyze the results, and to study their impact in a hypothetical practice, we used the data from [3] as reference for the spot diameters and the distances from S to D. These numbers are the most conservative available [3, 12]. Recall from the Introduction that, according to [3, 12], the diameters of the beam spots of well specified lasers, at focusing distances of 100 km and 250 km, are 15 cm and 11 cm, respectively.

[4] To clarify matters, let us look at an example. In [2, 4], the altitude 800 km is not considered, but rather 760 km and 831 km. Nevertheless, we chose 800 km, since the difference of 31 km only moderately alters the results. Moreover, the sequence $(200, 400, 800) = (2, 4, 8) \times 10^2 = (2, 2^2, 2^3) \times 10^2$ is covering the respective data range finer than the sequence $(2, 4, 8.31) \times 10^2$. Also, the altitudes $(200, 400, 800)$ are more representative for the location of the most LEO debris objects, according to the studies on the debris distribution provided in the catalogue of the United States Space Surveillance Network (SSN) (see e.g. [31]).

Thirteen figures are included in this section: Figs. 1 to 8 correspond to the group *'400 km'*, i.e., to the group of objects at 400 km in altitude at perigee. The eccentricity was 0.02. Note that the p-N corrections corresponding to this case are among the smallest in size, whereas Figs. 9 to 13 correspond to other cases, with corrections of medium size.

No other figures similar to Figs. 1 to 7, but corresponding to other groups, are provided in this section in order to keep concise the presentation. The fact is that the quantitative differences were relevant, but since the behavior was qualitatively similar, we decided not to repeat ourselves.

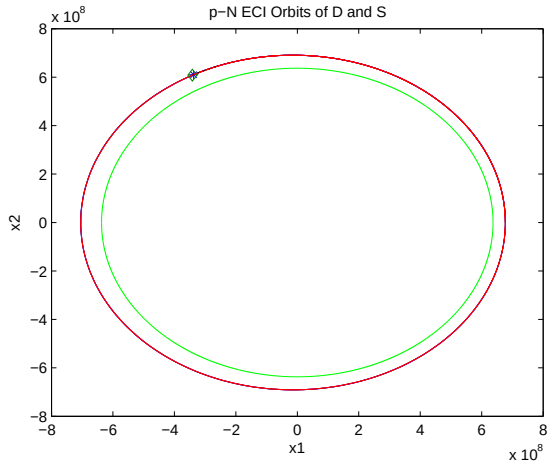

Figure 1: p-N ECI orbits of S and D.

Tables 1 and 2 contain the p-N corrections for the circular cases. The corrections in Table 1 were obtained without using the procedure in [15], while those in Table 2 correspond to the cases when the procedure was used.

Unlike those in Fig. 8, the corrections in Table 1 resulted in the largest among all discussed. As can be seen in this table, they reach 10 cm, i.e. the largest size of the objects considered, at distances well below 100 km. In turn, Table 2 shows that using the procedure in [15] resulted in a decrease in size of the corresponding corrections in Table 1.

Fig. 1 offers a global representation of the small eccentric ECI orbits of a typical object D and a hypothetical APT laser system S during a few revolutions about the Earth. The orbits cannot be clearly distinguished, since the picture was scaled so that the inner curve actually represents the Earth surface. Hence, for better visuality, only a few revolutions are displayed. Since the task of S is to push D into the atmosphere, D was assumed to be upper-followed by S until D was out of the effective range of the laser beam (assumed correctly directed up to at least 100 km).

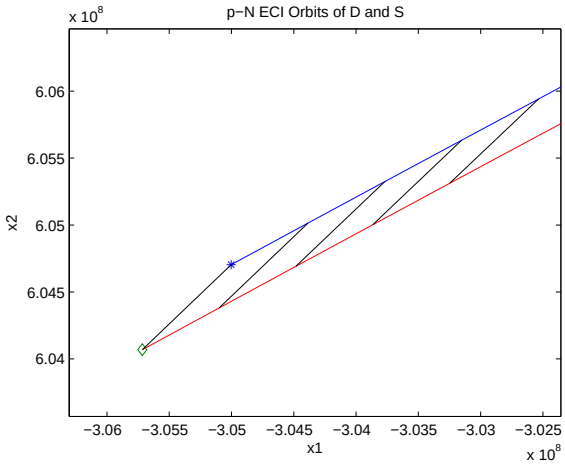

Figure 2: Close view of D and S orbits.

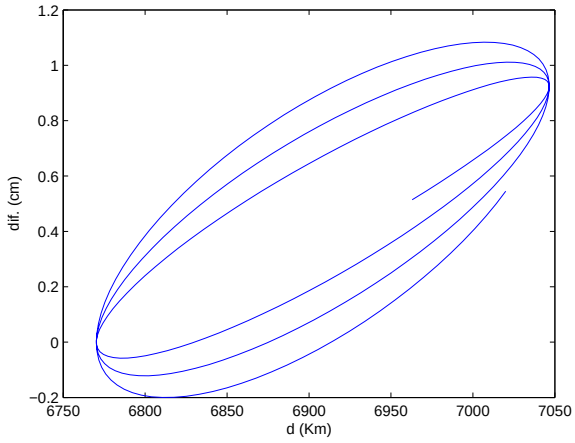

Figure 3: Diff. of dist. from ECI center to the N and p-N orbits of D.

The orbits of D and S, and the relative orbit of D with respect to S shown in Fig. 5 et seq., were computed by numerically integrating the p-N equations (3), (4). All numerical simulations were carried out in MATLAB using the standard routine `ode45` for the approximation of initial value problems (IVPs) in first order ordinary differential equations. Since the systems (3), (4) are of the second order, they were first transformed to related systems of the first order. The latter were then completed by a proper set of initial conditions. The `ode45` solver is based on the Dormand-Prince method [32], including two explicit RungeKutta methods of order four

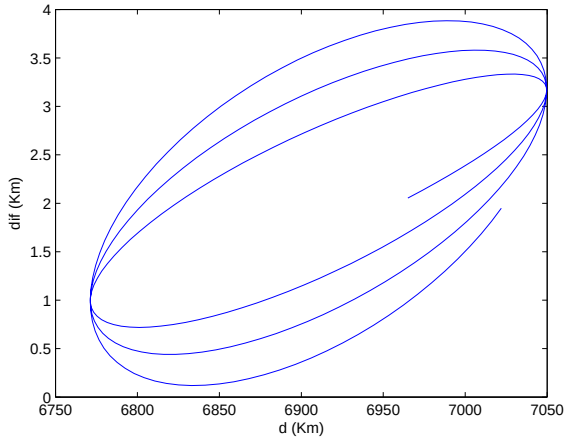

Figure 4: Diff. of dist. from ECI center to the p-N orbits of D and S.

and five and requiring six function evaluations per step. After each step, the difference between these solutions is taken to estimate the local error of the fourth order solution. This error estimate is then used to adapt the length of the step-size in such a way that the tolerance requirements provided by the user are satisfied. The Dormand-Prince method has seven stages, but it uses only six function evaluations per step because it has the First Same As Last property: the last stage is evaluated at the same point as the first stage of the next step. The coefficients of the method are chosen to minimize the error of the fifth order solution.

All calculation presented in the paper were carried out using the absolute and relative error control with the tolerance requirements set to $TOL_a = TOL_r = 10^{-11}$.

In a typical run, the whole interval of integration was split into 1000 equidistant subintervals. Starting from the first subinterval, an IVP was solved on an adapted grid until the end of the first subinterval was reached, and the code delivered an approximation of the prescribed accuracy. This procedure was repeated in the following subintervals, always starting with final solution values of the proceeding subinterval.

A typical run required a CPU time of 5 minutes. We stress that the experiments carried out here were not optimized for the *practical* production runs. Our aim was merely to illustrate the importance of the p-N corrections. For future industrial use, both algorithms and hardware have to be designed to considerably speed up the computations.

The computations were carried out until the distance between S to D was 150 km. The following initial conditions for the orbit of D were used: semi-major axis 2.258×10^{-2} s and eccentricity 0.02. In standard SI units this means that, while orbiting, the altitude of D over the Earth surface was about 400 km, cf. the circular case in [3]. To make sure that S performs the APT of D with satisfactory pointing accuracy, S was made to orbit on the orbital plane of D [15], in an orbit whose semi-major axis was by 1 km larger than the semi-axis of the orbit of D. To avoid possible collision, S was initially placed 5 km behind D.

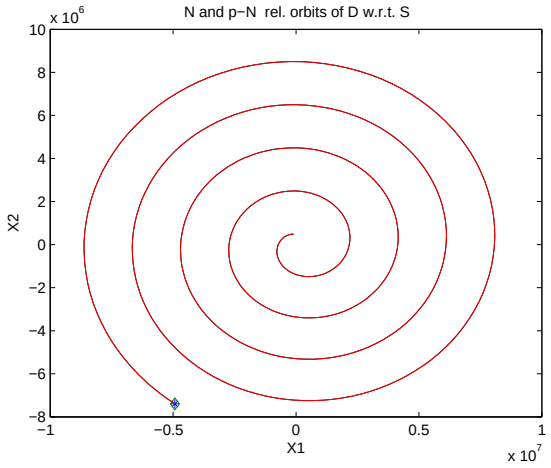

Figure 5: Relative N and p-N orbits of D w.r.t. S.

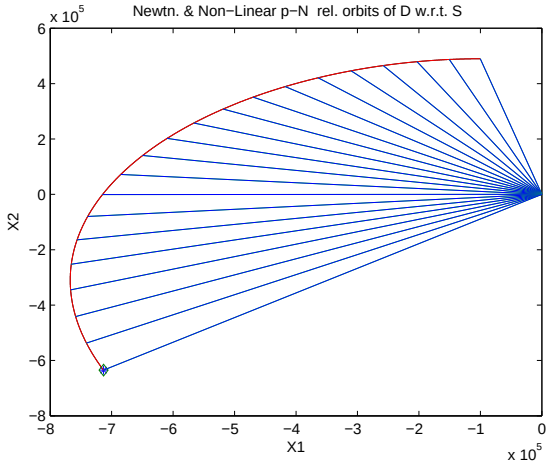

Figure 6: Partial view of N and p-N orbits of D w.r.t. S.

With respect to the orbital eccentricity of S and to the initial $S - D$ configuration, the eccentricity was fixed as prescribed in [15], therefore, having at perigee the same velocity D would have at perigee.

Finally, the integration of Eq. (3) for S and D were started simultaneously with S at perigee. Thus, the si-

multaneous computation of both orbits allowed to determine in real time the LOS of D from S.

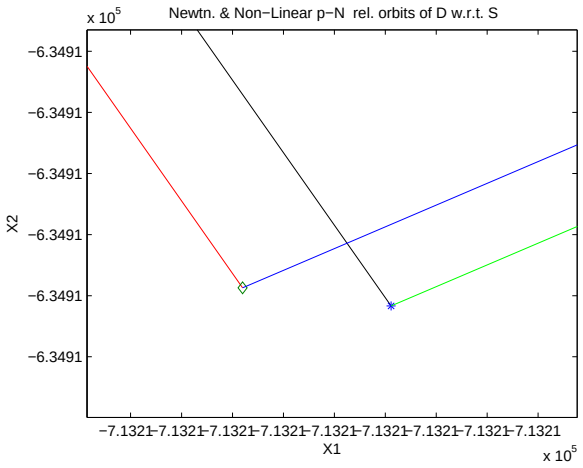

Figure 7: Close view of N and p-N orbits of D w.r.t. S.

The p-N orbits of S and D appear superposed simply because the distance between S and D is much smaller than the Earth radius. Hence, for better visibility, we enclose Fig. 2, which shows the last steps from Fig. 1 zoomed in.

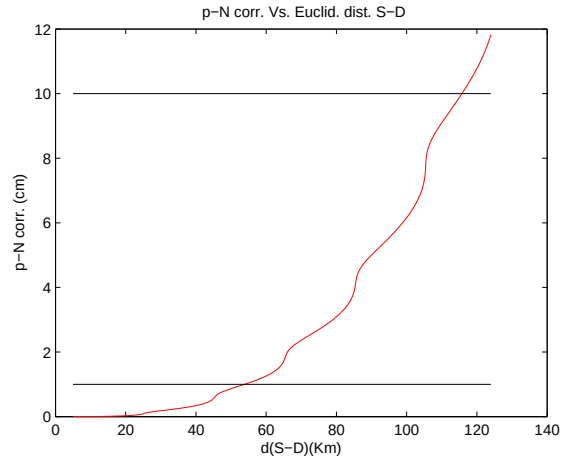

Figure 8: p-N corrections ($e_D = 0.02$;e_S adapt.,$alt_D = 400$ km.)

Fig. 2 now allows to realize that the orbit of S is always above the orbit of D with respect to the Earth, see the segments $[S, D]$ corresponding to the respective last steps. However, from the simple inspection of this figure, it is not possible to see one conclusion in [17]. This conclusion is that slight variations of the lengths and orientations of the segments $[S, D]$ with respect to those

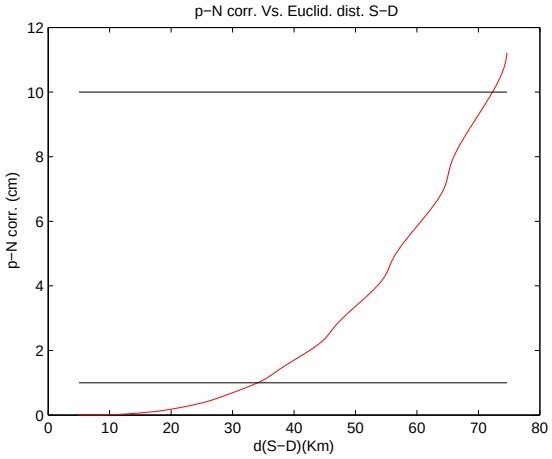

Figure 9: p-N corrections ($e_D = 0.02$, $e_S = 0.02$, $alt_D = 400$ km.)

of the Newtonian orbits are what make the differences in determining the coefficients in Eq. (4). Further computations are necessary indeed to derive the difference in the distances from the ECI center to the Newtonian and p-N positions of D, as well as the difference in the distances from the ECI center to the p-N positions of D and S.

In this context we remark, to complete the discussion below Eq. (4), that the segments $[S, D]$ defined in Section 3 depend on t, so that the values of the curvature of space along these segments, Eq. (A.12), determine the coefficients of Eq. (4). In fact, the equations for $[S, D]$, while S and D are orbiting according to (3), are

$$\bar{x}^\alpha(u) = (1-u)x^\alpha + ux^{\alpha'}, \quad 0 \le u \le 1,$$

where $x^\alpha(t)$ and $x^{\alpha'}(t)$, $\alpha = 1, 2, 3$, are the ECI p-N coordinates of D and S, respectively, see also Eqs. (A.10), (A.21). The results for the differences in distances corresponding to the last steps of the respective integrations are illustrated in Figs. 3 and 4.[5]

Finally, we stress that the differences discussed above are neither the distances between the Newtonian to the p-N positions of D, in the first case, nor the distances between the p-N positions of S and D, in the second case. In fact, the p-N relative orbit of D with respect to S was computed via Eq. (4), and its graph is shown in Fig. 5 (although, again, only after a few revolutions of D and S).

Fig. 5 also contains the Newtonian relative orbit of D w.r.t. S, which cannot be seen, since it is hidden behind the post-Newtonian orbit. This is so, because the

[5]Note that these orbits are not standard orbits in space. In part, they describe the problem as a dynamical system.

distance between these orbits is much smaller than the distance from S to D, regardless which orbit is considered to determine this distance.

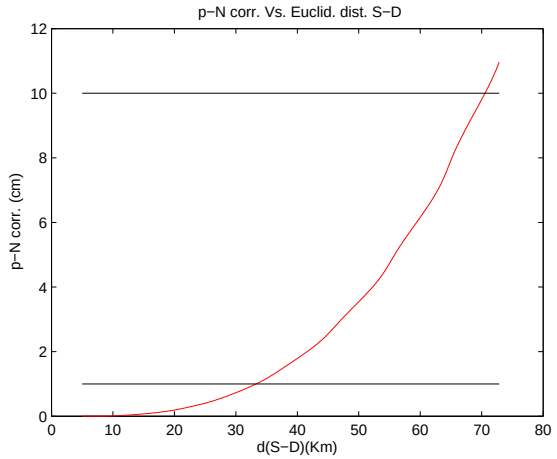

Figure 10: p-N corrections ($e_D = 0.01$, $e_S = 0.01$, $alt_D = 200$ km.)

Proceeding as before, we provided Figs. 6 and 7. Fig. 6 shows the evolution of $[S, D]$, counterclockwise due to the initial configuration $S - D$, and Fig. 7 shows the last steps of the integration of (4). More precisely, Fig. 7 is a zoom of the last arcs of the Newtonian and p-N orbits after the integration was terminated.

To clarify matters: the farthest orbit from S, the one on the left in Fig. 7, is the p-N orbit, and the nearest orbit, the one on the right, is the Newtonian orbit. S is out of the picture, on the right, so that only the D-ends of the respective segments can be seen as almost horizontal rays pointing to the left. Note that during the computation, we had in each step two segments $[S, D]$, one for the Newtonian relative position of D with respect to S and one for the corresponding post-Newtonian position.

We now formulate two final results:

1. The p-N corrections to the Newtonian positions, as seen from S, increasingly arrive at values between 1 cm and 10 cm for distances from S below 100 km.

2. Each wave in the curve of corrections corresponds to one revolution of D about S, again, as seen from S. The reference for this result can be found in Fig. 5.

These findings are adequately illustrated in Fig. 8. In this figure the horizontal lines correspond to 1 cm and 10 cm. They indicate the lower and upper bound for the size of the LEO objects considered. Since these lines are important, they are also pictured in the remaining figures, Figs. 9 to 13. From now on, we refer to them as the 1-size and the 10-size lines, respectively.

The results, so far encouraging, did not seem to be exclusive of the simulation setting discussed above. They rather suggested that similar corrections and waves, probably larger and smoother, could be obtained in the context of the other groups.

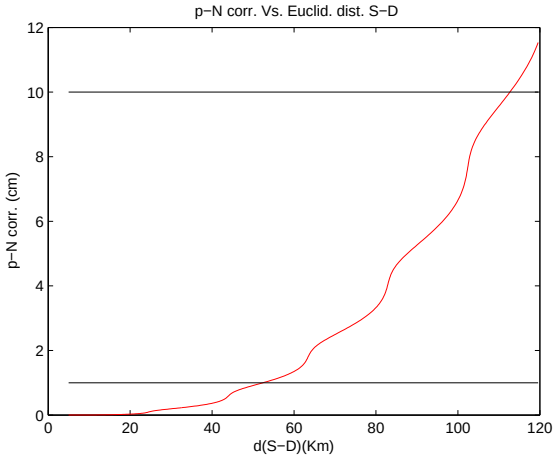

Figure 11: p-N corrections ($e_D = 0.01$, e_S adapt.,$alt_D = 200$ km.)

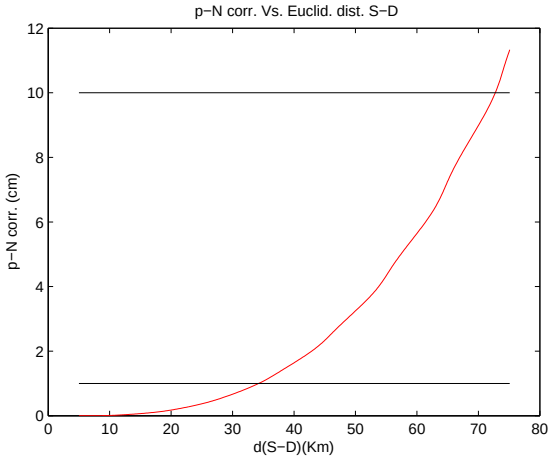

Figure 12: p-N corrections ($e_D = 0.01$, $e_S = 0.01$, $alt_D = 800$ km.)

Consequently, we continued the simulations starting with the same initial object D, but this time without implementing the procedure in [15].

It turned out that, for any working distance, the corrections became much larger than the corrections obtained previously, and the waves became much smoother. In fact, this time the 10-size line was reached well before the distance from S to D was 100 km, see Fig. 9.

It was clear that the results agreed with the general relativistic consequences that we assumed in searching

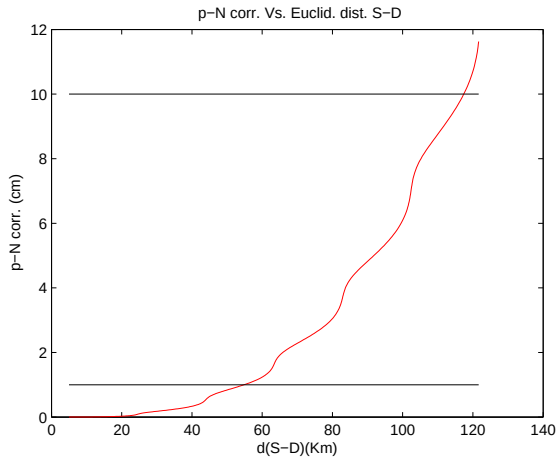

Figure 13: p-N corrections (e_D = 0.01, e_S adapt.,alt_D = 800 km.)

Alt. of D	800	400	200
S-D dist.	p-N corr.	p-N corr.	p-N corr.
40	1.68	1.78	1.82
60	5.84	6.18	6.36
80	13.92	14.82	15.28

Table 1: p-N corrections. e_S not adapted.

Alt. of D	800	400	200
S-D dist.	p-N corr.	p-N corr.	p-N corr.
40	0.35	0.37	0.39
60	1.33	1.40	1.43
80	3.42	3.58	3.75

Table 2: p-N corrections. e_S adapted.

for the p-N correction. They were due to the implementation of the procedure in [15] had made the eccentricity of S to take the value for which the relative transverse velocity of D w.r.t. S at perigee was practically zero, i.e., much smaller than the corresponding velocity when the procedure in [15] was not implemented.

To proceed with the investigations, we then chose objects D with different orbital eccentricities varying from 0.01, Figs. 10 to 13, down to zero. Moreover, we considered the altitude 800 km, 400 km, and 200 km at perigee. But the other orbital data were remained unchanged to allow for comparisons. Note from Figs. 10 to 13 that this time we started without implementing [15].

In all the cases similar results were observed, even after having considered substantial differences of ratios between the semi-major axis and eccentricities, so as after having modified the orientation of the orbits. The results followed the same pattern and showed the same behavior. In this respect the following facts were observed:

3. The smaller the eccentricities were, and the smaller the orbital distances to the atmosphere were, the faster the corrections increased, which is not surprising, according to General Relativity.

4. After implementing the procedure in [15] to adapt the eccentricity of S, the corrections decreased significantly. This result is very interesting, since it seems reasonable to deduce from it that this decrease will always occur.

In fact, the figure pairs, Figs. 10 and 11, and Figs. 12 and 13, are representative of the results for the groups *'200 km'* and *'800 km'*, respectively. In this context, we stress that while the 10-size line in Figs. 10 and 12 is reached before the distance between S and D is 80 km, the p-N corrections are still smaller than 6 cm at 100 km, see Figs. 11 and 13.

This means the following:

5. At distances even smaller that 100 km, the p-N correction to the Newtonian positions could be larger than all the objects considered, if the procedure in [15] is not implemented.

This completes our comments on the numerical simulations, with special focus on the circular cases discussed in the performance models in [1, 2, 3, 4].

We recapitulate the numerical findings in Tables 1 and 2. Table 1 corresponds to those simulations in which the procedure from [15] is not implemented, while Table 2 corresponds to the case when the procedure is implemented. There is no need for any further comment here, the numbers speak for themselves.

As a final remark, let us point out that among all the numerous simulations carried out during the testing, there was not a single one in which the corrections could be neglected.

5. Conclusions

Post-Newtonian corrections like those shown in this paper allow to increase the pointing accuracy required for the APT systems endowed with very narrow laser beams to push middle-sized LEO debris into the Earth atmosphere.

The corrections have been derived from Eq. (4). These equations are p-N equations for relative motions that account for the deviations of the LOS directions caused by the curvature of space along the paths that the laser beams are to travel along.

The size of the corrections is at the centimeter level, and often, the corrections result to be larger than the LEO objects involved.

Hence, even if all the classical perturbations are taken into account, including the finest, it will be still necessary to include the corrections discussed here. Otherwise, we will likely miss the aim to efficiently reach these dangerous objects, particularly, when they are among the smallest.

In consequence, there will be a clear need for a proper implementation of the point-ahead angles to shoot at these targets. In this context, an adequate adaptation of the APT procedure introduced in [15] could be suitable.

Finding this adaptation will be in the focus of our future work.

Appendix A.

The orbital equations for the LEO debris objects in ECI coordinates, $x^i(x^\alpha, t)$, as well as for the APT systems, are the geodesic equations

$$\frac{d^2x^i}{ds^2} = -\Gamma^i_{jk}\frac{dx^j}{ds}\frac{dx^k}{ds}, \tag{A.1}$$

where s corresponds to the respective proper time, and the Christoffel symbols, Γ^i_{jk}, to the ECI metric (1). For simplicity, we assume that the APT systems are inertial-guided, see (A.6). (Latin indices range from 1 to 4, and Greek, from 1 to 3).

As indicated in Section 2, in terms of the dimensionless parameter $\varepsilon \sim O(m/r) \sim O(v^2)$, the geometry of the space-time about the Earth in ECI coordinates x^i is given by (1), i.e., by

$$\begin{aligned} g_{\alpha\beta} &= \delta_{\alpha\beta} + \gamma_{\alpha\beta} + O(\varepsilon^2), \\ g_{\alpha 4} &= O(\varepsilon^{3/2}), \\ g_{44} &= -1 + \gamma_{44} + O(\varepsilon^2), \end{aligned} \tag{A.2}$$

where

$$\gamma_{\alpha\beta} = \frac{2m}{r}\frac{x_\alpha x_\beta}{r^2}, \quad \gamma_{44} = \frac{2m}{r}. \tag{A.3}$$

Here m is the mass of the Earth measured in seconds, v is the characteristic speed of the objects involved, it is dimensionless, and $r^2 = x_\alpha x^\alpha$, where r is also measured in seconds, see [29] and footnote 2.

Thus, the space part of the metric (A.2), $g_{\alpha\beta}$, is almost Euclidean, g_{44} is almost -1, and the Christoffel symbols, of second kind, Γ^i_{jk}, are

$$\Gamma^i_{jk} = \frac{1}{2}\left[\gamma_{i,jk} + \gamma_{ik,j} - \gamma_{jk,i}\right], \tag{A.4}$$

up to $O(\varepsilon^2)$, where $\gamma_{ij,k} = \partial\gamma_{ij}/\partial x^k$, etc.

Taking into account that during the APT action of S, the relative speed of D with respect to S is small as compared to the ECI velocity v^μ of S, we can see that ds'/ds (the relationship between the proper times s and s' of S and D, respectively) is approximately 1. Also, if the space-time trajectory L of S is given by $x^i(s) \equiv (x^\alpha(s), t(s))$, then, the unit tangent vector to L, say $\lambda^i_{(4)}(s)$, is given by

$$\begin{aligned} \lambda^\mu_{(4)}(s) &= v^\mu + O(\varepsilon^{3/2}), \\ \lambda^4_{(4)}(s) &= 1 + \frac{m}{r} + \frac{1}{2}v^2 + O(\varepsilon^2), \end{aligned} \tag{A.5}$$

where $v^2 = v_\mu v^\mu$.

The orthogonality conditions with respect to (A.2) for the tetrad of unit vectors $(\lambda^i_{(\alpha)}(s), \lambda^i_{(4)}(s))$ yield the components of the canonical inertial-guided system, $\lambda^i_{(\alpha)}(s)$, co-moving with S. Thus, we have

$$\lambda^\mu_{(\alpha)}(s) = \delta^\mu_\alpha + O(\varepsilon), \quad \lambda^4_{(\alpha)}(s) = v_\alpha + O(\varepsilon^{3/2}), \tag{A.6}$$

so that $\lambda^4_{(4)}$ in (A.5) gives dt/ds, which is the post-Newtonian relation between the ECI time coordinate and the proper time of S. According to the first in (A.6), the local (Fermi) space coordinates of D with respect to S are the Cartesian coordinates of D with respect to S up to $O(\varepsilon)$.

Let us denote these coordinates, as in Section 3, by $X^{(\alpha)}$. Then $X^{(\alpha)} = X_{(\alpha)} = (x^\alpha_D - x^\alpha_S) + O(\varepsilon) = ((x_\alpha)_D - (x_\alpha)_S) + O(\varepsilon)$, where $x^\alpha_D = (x_\alpha)_D$ and $x^\alpha_S = (x_\alpha)_S$ are the ECI space coordinates of D and S respectively. Obviously, the fourth coordinate of D with respect to S, $X^{(4)} = -X_{(4)}$, is s [29].

Since the classical post-Newtonian space-time as seen by S is given by, cf. [18, 30],

$$\begin{aligned} g_{(\alpha\beta)} &= \delta_{\alpha\beta} - \frac{1}{3}R_{(\alpha\mu\beta\nu)}|_S X^{(\mu)}X^{(\nu)} + O(\varepsilon^2), \\ g_{(\alpha 4)} &= O(\varepsilon^{3/2}), \\ g_{(44)} &= -1 - R_{(4\mu 4\nu)}|_S X^{(\mu)}X^{(\nu)} + O(\varepsilon^2), \end{aligned} \tag{A.7}$$

where $R_{(ijkl)}|_S$ is the Riemann tensor evaluated at S with the metric (A.2), the equations for the relative motion derived from this metric are appropriate only for objects D very close to S. In fact, according to the geodesic principle, these equations are

$$\frac{d^2X_{(\alpha)}}{ds^2} = -R_{(\alpha 4\beta 4)}|_S X^{(\beta)}. \tag{A.8}$$

Hence, to formulate equations valid for objects orbiting far from S a suitable metric is required. In this context, we use Synge's metric, since it accounts for

the value of $R_{(ijkl)}$ along the straight line segments that connect S and D, while S and D are orbiting the Earth. These segments are the LOS from S to D up to the $O(\varepsilon)$.

If x^α and $x^{\alpha'}$ are the ECI coordinates of S and D at s respectively, and $(X^{(\alpha)}, X^{(4)})$ the coordinates of D with respect to S and $\lambda^\mu_{(\alpha)}$ at s, then the Synge's metric at D is given by [29]

$$\begin{aligned} \bar{g}_{(\alpha\beta)} &= \delta_{\alpha\beta} + 2\bar{h}_{(\alpha\beta)} + O(\varepsilon^2), \\ \bar{g}_{(\alpha 4)} &= O(\varepsilon^{3/2}), \\ \bar{g}_{(44)} &= -1 + 2\bar{h}_{(44)} + O(\varepsilon^2), \end{aligned} \tag{A.9}$$

where

$$\begin{aligned} \bar{h}_{(\alpha\beta)} &= \frac{3}{2} X^{(\mu)} X^{(\nu)} \int_0^1 (1-u) u S_{(\alpha\beta\mu\nu)} du, \\ \bar{h}_{(44)} &= \frac{3}{2} X^{(\mu)} X^{(\nu)} \int_0^1 (1-u) S_{(44\mu\nu)} du. \end{aligned} \tag{A.10}$$

The line integrals above are computed along the segments $\bar{x}^\alpha(u) = (1-u)x^\alpha + u x^{\alpha'}$, $0 \le u \le 1$.

We note that $S_{(abcd)}$ in (A.10) is the symmetrized Riemann tensor at $\bar{x}^\alpha(u)$ evaluated with the metric (A.2). Hence, the value of $S_{(abcd)}$ to be used in (A.10) is

$$S_{(abcd)}(\bar{x}^\mu(u)) = -\frac{1}{3}\Big(R_{(acbd)} + R_{(adbc)}\Big)\Big(\bar{x}^\mu(u)\Big), \tag{A.11}$$

where $R_{(acbd)}$ is the Riemann tensor at $\bar{x}^\alpha(u)$ evaluated with (A.2). Its components at $\bar{x}^\alpha(u)$ are

$$R_{(\alpha 4 \gamma 4)}(\bar{x}^\mu(u)) = -m\left(\frac{3\bar{x}_\alpha(u)\bar{x}_\gamma(u)}{\bar{r}(u)^5} - \frac{\delta_{\alpha\gamma}}{\bar{r}(u)^3}\right), \tag{A.12}$$

where $\bar{r}(u)^2 = \bar{x}_\mu(u)\bar{x}^\mu(u)$. Note that $R_{(\alpha 4 \gamma 4)}$ are $O(\varepsilon)$.

We now follow Synge's procedure to model the motion of D with respect to S [29].

Let L be the space-time evolution line of S, and L', the evolution of D. Then, according to the initial hypothesis, L and L' are geodesics. Let us also consider for each event P' of L' the event P of L, simultaneous to P' as measured by the clock carried on by S. If the coordinates of D with respect to S at s are $X^{(i)} \equiv (X^{(\alpha)}, X^{(4)})$, so that $X^{(4)} = s$, then the coordinates of P are $(0, s)$. Let us finally assume that the ECI coordinates of P and P' are $x^i \equiv (x^\alpha, x^4)$ and $x^{i'} \equiv (x^{\alpha'}, x^{4'})$, and x^4 and $x^{4'}$ are t and t', respectively.

We know that L' is determined by P' and the unit tangent to L'. Therefore, in order to find the equations for L', we shall write $X^{(\alpha)}(s)$ in terms of the length of the straight-line segment $\Gamma(\bar{x}^i(u))$ that joins P and P'.

Now, since P and P' run along L and L', this length is a function of x^i and $x^{i'}$. Hence, we can express the second derivative of $X^{(\alpha)}$ with respect to s in terms of the derivatives of this function.

With $\Omega(x^i, x^{i'})$ defined by the line integral

$$\Omega(x^i, x^{i'}) = \frac{1}{2}\int_P^{P'} g_{ij}\frac{d\bar{x}^i}{du}\frac{d\bar{x}^j}{du}du, \tag{A.13}$$

we have $X^{(\alpha)} = X_{(\alpha)} = -\Omega_i \lambda^i_{(\alpha)}$, with $\Omega_i \lambda^i_{(4)} = 0$, where g_{ij} are given in (A.2), $\lambda^i_{(\alpha)}$ are given in (A.6), and $\Omega_i = \partial\Omega(x^i, x^{i'})/\partial x^i$.

The condition for L to be geodesic is $d\lambda^i_{(\alpha)}/ds = 0$, and the differentiation of $X^{(\alpha)}$ gives

$$\frac{dX_{(\alpha)}}{ds} = -\Omega_{ij}\lambda^i_{(\alpha)}\lambda^j_{(4)} - \Omega_{ij'}\lambda^i_{(\alpha)}\lambda^{j'}_{(4)}, \tag{A.14}$$

where $\Omega_{ij} = \partial^2\Omega/\partial x^j \partial x^i$, $\Omega_{ij'} = \partial^2\Omega/\partial x^{j'}\partial x^i$, and $\lambda^{j'}_{(4)} = dx^{i'}/ds$. Therefore, the second derivatives read

$$\begin{aligned} \frac{d^2X_{(\alpha)}}{ds^2} &= -\Omega_{ijk}\lambda^i_{(\alpha)}\lambda^j_{(4)}\lambda^k_{(4)} - \Omega_{ijk'}\lambda^i_{(\alpha)}\lambda^j_{(4)}\lambda^{k'}_{(4)} \\ &-\Omega_{ij'k}\lambda^i_{(\alpha)}\lambda^{j'}_{(4)}\lambda^k_{(4)} - \Omega_{ij'k'}\lambda^i_{(\alpha)}\lambda^{j'}_{(4)}\lambda^{k'}_{(4)}, \end{aligned} \tag{A.15}$$

where $\Omega_{ijk} = \partial^3\Omega/\partial x^k\partial x^j\partial x^i$, $\Omega_{ijk'} = \partial^3\Omega/\partial x^{k'}\partial x^j\partial x^i$, $\Omega_{ij'k} = \partial^3\Omega/\partial x^k\partial x^{j'}\partial x^i$, and $\Omega_{ij'k'} = \partial^3\Omega/\partial x^{k'}\partial x^{j'}\partial x^i$.

Now, by (A.5),

$$\lambda^\mu_{(4)} = v^\mu + O(\varepsilon^{3/2}), \qquad \lambda^4_{(4)} = 1 + O(\varepsilon), \tag{A.16}$$

$$\lambda^{\mu'}_{(4)} = v^{\mu'} + O(\varepsilon^{3/2}), \qquad \lambda^{4'}_{(4)} = 1 + O(\varepsilon), \tag{A.17}$$

where $v^{\mu'}$ is the ECI velocity of D at s. Then (A.15) becomes

$$\frac{d^2X_{(\alpha)}}{ds^2} = -\Omega_{(\alpha 44)} - \Omega_{(\alpha 44')} - \Omega_{(\alpha 4' 4)} - \Omega_{(\alpha 4' 4')}, \tag{A.18}$$

where $\Omega_{(\alpha 44)} = \Omega_{ijk}\lambda^i_{(\alpha)}\lambda^j_{(4)}\lambda^k_{(4)}$, etc.

The final step is to compute the third derivatives of Ω and insert them into (A.18). A straightforward calculation yields

$$\begin{aligned} -\Omega_{(\alpha 44)} = \Omega_{(\alpha 44')} = \Omega_{(\alpha 4' 4)} &= X^{(\gamma)}\int_0^1 (1-u)^2 R_{(\alpha 4 \gamma 4)} du, \\ \Omega_{(\alpha 4' 4')} &= 2X^{(\gamma)}\int_0^1 u^2 R_{(\alpha 4 \gamma 4)} du \\ -X^{(\mu)}X^{(\nu)}&\int_0^1 (1-u)u^2 \frac{\partial R_{(\mu 4 \nu 4)}}{\partial x^\alpha} du, \end{aligned} \tag{A.19}$$

so that (A.18) becomes

$$\frac{d^2X_{(\alpha)}}{ds^2} = -X^{(\gamma)} \int_0^1 (1 - 2u + 3u^2) R_{(\alpha 4 \gamma 4)} du$$

$$+X^{(\mu)} X^{(\nu)} \int_0^1 (1-u) u^2 \frac{\partial R_{(\mu 4 \nu 4)}}{\partial x^\alpha} du. \qquad \text{(A.20)}$$

This finally yields the equations in (4) with

$$A_{\alpha\gamma} = -\int_0^1 (1 - 2u + 3u^2) R_{(\alpha 4 \gamma 4)} du,$$

$$\bar{A}_{\mu\nu} = \int_0^1 (1-u) u^2 \frac{\partial R_{(\mu 4 \nu 4)}}{\partial x^1} du,$$

$$\bar{B}_{\mu\nu} = \int_0^1 (1-u) u^2 \frac{\partial R_{(\mu 4 \nu 4)}}{\partial x^2} du,$$

$$\bar{C}_{\mu\nu} = \int_0^1 (1-u) u^2 \frac{\partial R_{(\mu 4 \nu 4)}}{\partial x^3} du, \qquad \text{(A.21)}$$

and $R_{(\mu 4 \nu 4)}$, cf. (A.12).

Note that the integrals in (A.21) have to be computed taking into account that the ECI post-Newtonian locations of S and D are given by Eq. (3).

References

[1] A. V. Avdeev, A. S. Bashkin, B. I. Katorgin, M. Parfen'ev, About possibilities of clearing near-Earth space from dangerous debris by a spaceborne laser system with an autonomous cw chemical HF laser, Quantum Electron. 41 (7) (2011) 669–674.

[2] C. R. Phipps, L'adroit–a spaceborne ultraviolet laser system for space debris clearing, Acta Astronaut. 104 (1) (2014) 243–255.

[3] S. Shen, X. Jin, C. Hao, Cleaning space debris with a space-based laser system, Chin. J. Aeronaut. 27 (4) (2014) 805–811.

[4] M. Schmitz, S. Fasoulas, J. Utzmann, Performance model for space-based laser debris sweepers, Acta Astronaut. 115 (2015) 376–383.

[5] J. W. Campbell, Using lasers in space: laser orbital debris removal and asteroid deflection, Center for Strategy and Technology, Air Univ. Maxwell Air Force Base, 2000.

[6] M. Ansdell, Active space debris removal: Needs, implications, and recommendations for today's geopolitical environment, J. Public Int. Affairs 21 (2010) 7–22.

[7] B. Greene, Y. Gao, C. Moore, Y. Wang, A. Boiko, Laser tracking of space debris, in: 13th International Workshop on Laser Ranging Instrumentation, Washington DC, 2002.

[8] S. H Choi, R. S Pappa, Assessment study of small space debris removal by laser satellites, Recent Pat. Space Tech. 2 (2) (2012) 116–122.

[9] M. K. Thind, C. Lokesh, Removal of space debris using laser, Adv. Aerosp. Sci. Appl. 3 (2) (2013) 107–112.

[10] N. Thiry, M. Vasile, Deflection of uncooperative targets using laser ablation, Proc. SPIE, 2015.

[11] A. Gibbings, M. Vasile, J.-M. Hopkins, A. Wayman, S. Eckersley, I. A. Watson, A space-based laser system for the deflection and manipulation of near Earth asteroids, in: Int. High Power Laser Ablation and Beamed Energy Propulsion Symposium, HPLA/BEP, 2014.

[12] C. R. Phipps, C. Bonnal, A spaceborne, pulsed UV laser system for re-entering or nudging LEO debris, and re-orbiting GEO debris, Acta Astronaut. 118 (2016) 224–236.

[13] M. Shan, J. Guo, E. Gill, Review and comparison of active space debris capturing and removal methods, Prog. Aerosp. Sci. 80 (2016) 18–32.

[14] O. Montenbruck, E. Gill, Satellite orbits: models, methods and applications, Springer Science & Business Media, 2012.

[15] J. M. Gambi, M. L. Garcia del Pino, Autonomous shooting at middle size space debris objects from space-based APT laser systems, Acta Astronaut. 131 (2017) 83–91.

[16] J. M. Gambi, M. L. Garcia del Pino, M. C. Rodriguez-Teijeiro, Non-linear post-Newtonian equations for the motion of designated targets with respect to space based APT laser systems, in: 19th European Conference on Mathematics for Industry, 2016, p. 24.

[17] J. M. Gambi, M. L. Garcia del Pino, J. Gschwindl, E. B. Weinmüller, Post-Newtonian corrections to the Newtonian predictions for the motion of designated targets with respect to space based APT laser systems, in: 19th European Conference on Mathematics for Industry, 2016, p. 25.

[18] M. H. Soffel, Relativity in Astrometry, Celestial Mechanics and Geodesy. Astronomy and Astrophysics Library, Springer-Verlag, 1989.

[19] J. M. Gambi, M. L. Garcia del Pino, Post-newtonian equations of motion for inertial guided APT systems, WSEAS Trans. Math. 14 (2015) 256–264.

[20] H. Moritz, B. Hofmann-Wellenhof, Geometry, relativity, geodesy, Wichmann Karlsruhe, 1993.

[21] N. Ashby, Relativity in the global positioning system, Living Rev. Relativ. 6 (1) (2003) 1–42.

[22] T. B. Bahder, Navigation in curved space–time, Amer. J. Phys. 69 (3) (2001) 315–321.

[23] T. B. Bahder, Clock Synchronization and Navigation in the Vicinity of the Earth, Nova Sci. Pub. Inc., 2009.

[24] N. Ashby, P. L. Bender, Measurement of the Shapiro time delay between drag-free spacecraft, in: Lasers, Clocks and Drag-Free Control, Springer, 2008, pp. 219–230.

[25] J. M. Gambi, M. C. Rodriguez-Teijeiro, M. L. Garcia del Pino, M. Salas, Shapiro time delay within the geolocation problem by TDOA, IEEE T. Aero. Elec. Sys. 47 (3) (2011) 1948–1962.

[26] J. M. Gambi, J. Clares, M. L. Garcia del Pino, FDOA post-Newtonian equations for the location of passive emitters placed in the vicinity of the Earth, Aerosp. Sci. Technol. 46 (2015) 137–145.

[27] J. M. Gambi, J. Clares, M. C. Rodriguez-Teijeiro, Post-Newtonian geolocation of passive radio transmitters by TDOA and FDOA, in: 18th European Conference on Mathematics for Industry, 2014, p. 176.

[28] J. M. Gambi, M. C. Rodriguez-Teijeiro, M. L. Garcia del Pino, Newtonian and post-Newtonian passive geolocation by TDOA, Aerosp. Sci. Technol. 51 (2016) 18–25.

[29] J. Synge, Relativity: The General Theory, North-Holland Pub. Co., 1960.

[30] K. Nordtvedt Jr, Post-Newtonian metric for a general class of scalar-tensor gravitational theories and observational consequences., Astrophys. J. 161 (1970) 1059.

[31] D. Shoots, Orbital Debris Quarterly News, Vol. 18, Issue 4, in: Debi Shoots (Ed.), National Aeronautics and Space Administration, October 2014.

[32] J. R. Dormand, P. J. Prince, A family of embedded runge-kutta formulae, J. Comput. Appl. Math. 6 (1) (1980) 19–26.